PNAS RESEARCH ARTICLE | PHYSICS

Discovery of charge order in a cuprate Mott insulator

Mingu Kang[a,b,1], Chao C. Zhang[c,1], Enrico Schierle[d], Stephen McCoy[e,f], Jiarui Li[a], Ronny Sutarto[g], Andreas Suter[h], Thomas Prokscha[h], Zaher Salman[h], Eugene Weschke[d], Shane Cybart[e,f], John Y. T. Wei[c,2], and Riccardo Comin[a,2]

Edited by J.C. Davis, University of Oxford, Oxford, United Kingdom; received February 9, 2023; accepted June 12, 2023

Copper oxide superconductors universally exhibit multiple forms of electronically ordered phases that break the native translational symmetry of the CuO_2 planes. In underdoped cuprates with correlated metallic ground states, charge/spin stripes and incommensurate charge density waves (CDWs) have been experimentally observed over the years, while early theoretical studies also predicted the emergence of a Coulomb-frustrated 'charge crystal' phase in the very lightly doped, insulating limit of CuO_2 planes. Here, we search for signatures of CDW order in very lightly hole-doped cuprates from the 123 family $RBa_2Cu_3O_{7-\delta}$ (RBCO; R: Y or rare earth), by using resonant X-ray scattering, electron transport, and muon spin rotation measurements to resolve the electronic and magnetic ground states fully. Specifically, Pr is used to substitute Y at the R-site to systematically suppress the superconductivity and access the extremely low hole-doping regime of the cuprate phase diagram without changing the oxygen stoichiometry. X-ray scattering data taken on Pr-doped YBCO thin films reveal an in-plane CDW order that follows the same linear evolution of wave vector versus hole concentration as oxygen-underdoped YBCO but extends all the way to the insulating and magnetically ordered Mott limit. Combined with the recent observation of charge crystal phase on an insulating surface of $Bi_2Sr_2CaCu_2O_{8+z}$, our results in RBCO suggest that this electronic symmetry breaking is universally present in very lightly doped CuO_2 planes. These findings bridge the gap between the Mott insulating state and the underdoped metallic state and underscore the prominent role that Coulomb-frustrated electronic phase separation plays among all cuprates.

cuprates | intertwined orders | charge crystals

Significance

Charge density waves (CDWs) are a collective state of quantum matter where the conduction electrons in a metal organize themselves in a spatially-modulated fashion. In copper oxides, CDWs are known to coexist and compete with high-temperature superconductivity, making their explication essential for a complete description of unconventional superconductivity. Using a unique combination of X-ray, muon, and transport probes, we searched for CDWs in the yet-unexplored limit of very lightly-doped cuprates. Contrary to commonly-accepted knowledge of these phenomena in cuprates, we find that a spatially-modulated electronic state can exist in the Mott-insulator phase that is precursive to the superconductivity. This observation challenges our theoretical understanding of CDWs in cuprates and provides an important indication that they originate from strong-correlation physics.

Following the discovery of high-temperature superconductivity in cuprates (1, 2), early theoretical studies proposed that multiple forms of electronic symmetry-breaking exist in lightly doped Mott insulators (3–6). These theoretical predictions were first confirmed by the discovery of charge and spin stripes in $La_{1.48}Nd_{0.4}Sr_{0.12}CuO_4$ (7). During the last decade, multiple forms of these symmetry-breaking states have been discovered in all cuprate high-temperature superconductors (8–17). In many cases, these emergent phases are intertwined with superconductivity (18–20) in ways that have been investigated from multiple perspectives (21–28).

The driving mechanisms behind electronic order in the CuO_2 planes have been the subject of longstanding questions that are essential for the understanding of quantum matter and high-temperature superconductivity in cuprates (29). However, a consensus on the origin of electronic order has not formed fully, partly because of key phenomenological differences between the cuprate families of $YBa_2Cu_3O_{7-y}$ (123) $Bi_2Sr_2CaCu_2O_{8+z}$ (2212), and doped La_2CuO_4 (214). In the latter, charge order cohabits with static spin order to form electronic stripes characterized by Coulomb-frustrated real-space phase separation and a spatial periodicity directly correlated with the hole concentration. However, this "real-space Coulomb frustration" scenario has not found wide applicability in other cuprate families, because of a competing "momentum-space instability" hypothesis. This alternative model posits that scattering between itinerant states mediated by strong antiferromagnetic fluctuations is the origin of electronic order in cuprates (23, 24, 26, 28).

A clear discriminant between these two frameworks is the existence of an electronic crystal phase in lightly doped and insulating CuO_2 planes. This state has been predicted under the real-space scenario (30) but is incompatible with the momentum-space scenario, since charge order requires a correlated metallic state with low-energy quasiparticles and a Fermi surface in the latter model. A recent scanning tunneling spectroscopy study (31) observed periodic spatial modulations of the electronic density of states on an insulating surface of Bi-2212, providing fresh evidence for an electronic crystal state in lightly doped CuO_2 planes. This study demonstrates that the phenomenology of

The authors declare no competing interest.

This article is a PNAS Direct Submission.

[1]M.K. and C.C.Z. contributed equally to this work.

[2]To whom correspondence may be addressed Email: rcomin@mit.edu or wei@physics.utoronto.ca.

This article contains supporting information online at https://www.pnas.org/lookup/suppl/doi:10.1073/pnas.2302099120/-/DCSupplemental.

Published July 17, 2023.

electronic orders in underdoped Bi-based cuprates needs to be understood on the basis of the real-space Coulomb frustration picture. If also confirmed in the insulating regime of Y-based cuprates, the existence of an electronic crystal state would significantly impact our understanding of electronic orders in the CuO_2 planes among all cuprates.

To address this question, we turn our attention to the 123 family of $RBa_2Cu_3O_{7-y}$ compounds (RBCO; R: Y or rare earth) (2). Among cuprate superconductors, the RBCO family is one of the most widely studied, owing to their relatively high critical temperature (T_c) and the ability to change their hole concentration (p) by varying the oxygen stoichiometry (y) (2, 32). This ability is uniquely enabled by the crystal structure of RBCO, with the CuO chain layers providing a charge reservoir for the CuO_2 planes, which form a bilayer around the spacer rare-earth layer (Fig. 1*A*). To sidestep challenges in controlling the oxygen stoichiometry in the chain layer at very low hole doping levels, we take an alternative route of using Pr-substitution at the Y site in nearly fully oxygenated ($y \ll 1$) samples of $Y_{1-x}Pr_xBa_2Cu_3O_{7-y}$ (YPrBCO) to underdope the material (known phase diagram is shown in Fig. 1*C*). In YPrBCO, the concentration of mobile carriers in the CuO_2 planes is controlled using the unique ability of low-energy Pr 4f orbitals to effectively sequester holes from Cu $3d_{x^2-y^2}$–O $2p_\sigma$ states (33–35). Namely, Pr $4f_{z(x^2-y^2)}$ orbitals hybridize with O $2p_\pi$ orbitals to form a Pr $4f_{z(x^2-y^2)}$–O $2p_\pi$ state (36), which binds mobile holes from the CuO_2 planes to the Pr sites (37). Fully substituted PrBCO ($x = 1$) is known to be insulating and antiferromagnetic (Fig. 1*C*), therefore providing an ideal platform to study electronic orders down to the Mott limit. In contrast, substitution of other rare earth elements has marginal impacts on the electronic properties of YBCO (35), and we also measured $HoBa_2Cu_3O_{7-y}$ (HoBCO) and $EuBa_2Cu_3O_{7-y}$ (EuBCO), as non-Pr controls.

Using resonant soft X-ray scattering (RXS) at the Cu-L_3 ($2p \rightarrow 3d$) and Pr-M_5 ($3d \rightarrow 4f$) edges on RBCO thin films, we reveal an in-plane charge density wave (CDW) state across the phase diagram of YPrBCO, fully extended from the superconducting ($x = 0$, 0.275, 0.5) regime to the insulating regime ($x = 0.75$) and the Mott limit ($x = 1$). In PrBCO, our observation of a CDW in the absence of a Fermi surface and its coexistence with static Neel order crucially underscores the need for Coulomb frustration to support charge order in RBCO.

Results

We first present the basic characterization of YPrBCO thin films with Pr contents $x = 0$, 0.275, 0.5, 0.75, and 1. The films were grown using pulsed laser-ablated deposition (PLD) and

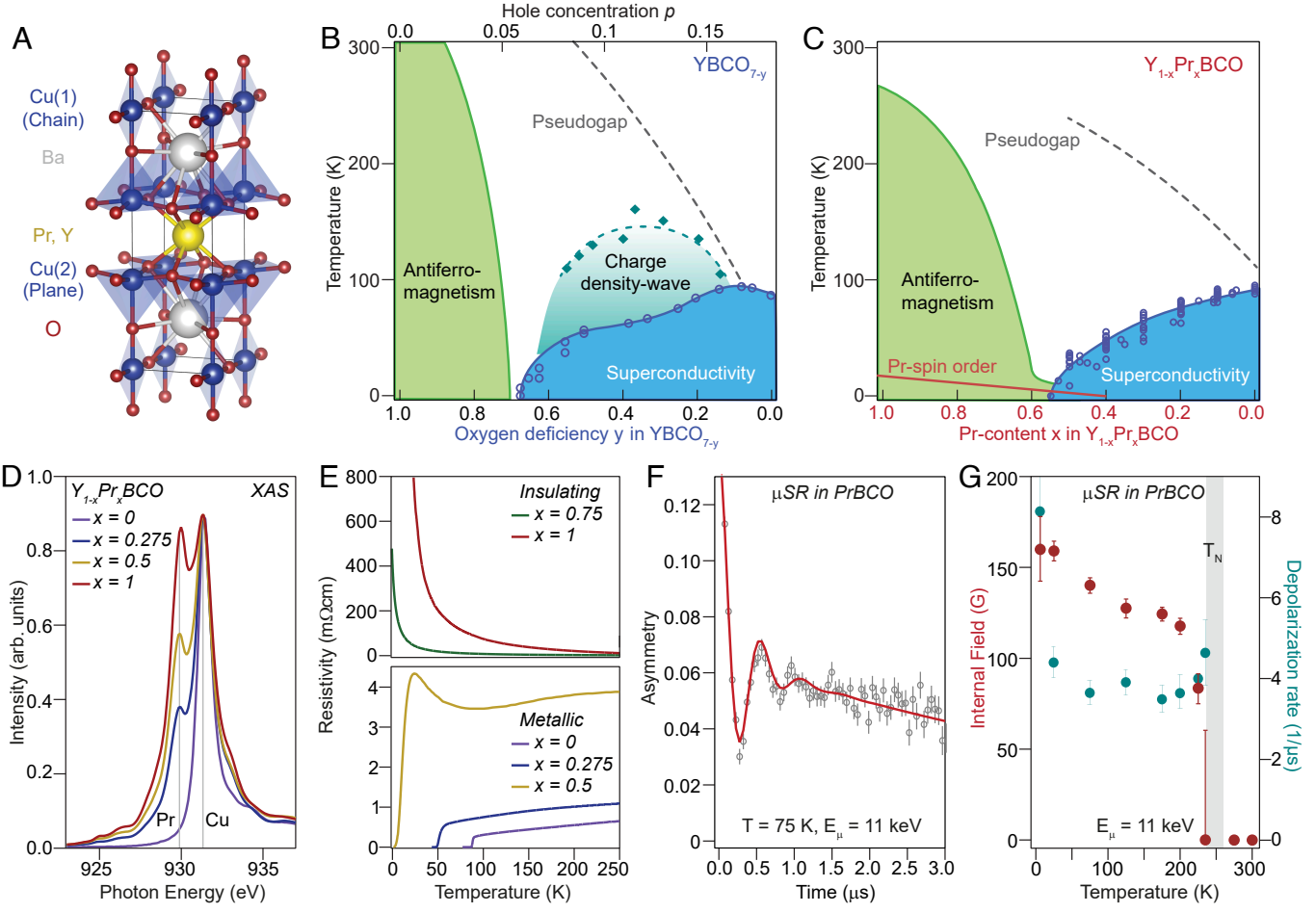

Fig. 1. Experimental characterization of YPrBCO. (*A*) Crystal structure of the unit cell, containing a CuO_2-(Y,Pr)-CuO_2 bilayer. (*B* and *C*) Known phase diagrams of $YBCO_{7-y}$ and YPrBCO, respectively. The phase boundaries shown are based on data adapted from refs. 10, 32, and 38. (D) X-ray absorption spectra of YPrBCO films, showing two main peaks at 931.3 eV and 930 eV for the Cu-L_3 and Pr-M_5 edges, respectively. (*E*) Resistivity vs. temperature characteristics of YPrBCO films; top and bottom panels are plotted on different vertical scales. (*F*) Asymmetry spectrum of μSR measured on a PrBCO film at 75 K. (*G*) Temperature dependences of the internal field and depolarization rate, determined from fitting the μSR asymmetry spectra at various temperatures. The gray bar indicates the onset of magnetic order at $T_N \approx 250$ K. A magnetic volume fraction close to 100% is deduced from weak transverse field ($B_{ext} = 75G$) measurements.

structurally confirmed using X-ray diffraction (XRD). Details of the growth and characterization processes are presented in *Material and Methods*. X-ray absorption spectra (XAS) are shown in Fig. 1*D*. Two prominent absorption peaks are observed at 931.3 eV and 930.0 eV, corresponding to the Cu-L_3 and Pr-M_5 resonances respectively. The intensity of the Pr-M_5 peak grows in accordance with higher Pr content x.

Transport properties of the YPrBCO films are displayed in Fig. 1*E*. The resistivity vs. temperature curves of the films are consistent with those reported in the literature (33, 38–40). The midpoint T_c of the YBCO ($x = 0$) film is $\approx$ 90 K, in agreement with prior reports (10, 32, 41). With Pr substitution, the midpoint T_c is reduced to 55 K for $x = 0.275$ and then to 12 K for $x = 0.5$. For the latter, an upturn in resistivity is manifested at low temperatures, signaling a metal-insulator transition. The films with $x = 0.75$ and $x = 1$ both show insulating behavior, the latter being more resistive than the former. The room-temperature resistivity of the PrBCO ($x = 1$) film is $\approx$11 mΩ·cm, similar to that of lightly Ca-doped $YBa_2Cu_3O_6$ (42, 43).

We also performed zero-field muon spin rotation (ZF-μSR) measurements to characterize the magnetic properties of the insulating end compound PrBCO. As shown in Fig. 1*F*, the ZF-μSR time spectrum at 75 K exhibits oscillations that are indicative of the presence of static magnetic order in the PrBCO film. By fitting the ZF-μSR spectra using a standard function (see *Material and Methods* for detail), we extract the internal field and depolarization rate as a function of temperature in Fig. 1*G*. The internal field shows a sharp onset of static spin order at $T_N \approx 250$ K, where the decay rate also peaks. The latter shows a second rise below $\sim$25 K due to the additional ordering of Pr magnetic moments. Both the Cu and Pr ordering temperatures are consistent with those reported in previous studies (38, 44). Overall, the electronic and magnetic properties of the YPrBCO thin films studied here are quantitatively consistent with previous reports (34, 38, 45, 46), confirming that Pr-substitution effectively underdopes the CuO_2 planes down to the magnetically ordered, insulating limit (Fig. 1*C*).

Fig. 2*A* shows a series of RXS scans of PrBCO along the Cu-O bond direction (Q_x), taken over a range of photon energies covering Cu-3*d* (931.3 eV) and Pr-4*f* (930.0 eV) resonances. On top of a smooth background due to fluorescence and the tail of a specular reflection near $Q_x = 0$, a prominent two-peak structure appears between $|Q_x| \approx 0.2$ and 0.4 r.l.u. Gaussian fits of the RXS profile reveal that the diffraction signatures are composed of two distinct peaks centered at 0.36 and 0.28 r.l.u (see *SI Appendix*, Fig. S1 for line shape analysis). The full-width-at-half-maximum in both cases is estimated to be $\approx$0.06–0.08 r.l.u., reflecting the presence of short-range charge correlations with a spatial coherence length $\xi \approx$ 6–7 unit cells or $\approx$ 25–30 Å. Both diffraction peaks originate from ordering of the charge degrees of freedom as confirmed by the photon polarization analysis (*SI Appendix*, Fig. S2) (8). Additional azimuthal angle-dependent experiments indicate that the double-peak structure appears only along the Cu-O bond direction (*SI Appendix*, Fig. S3).

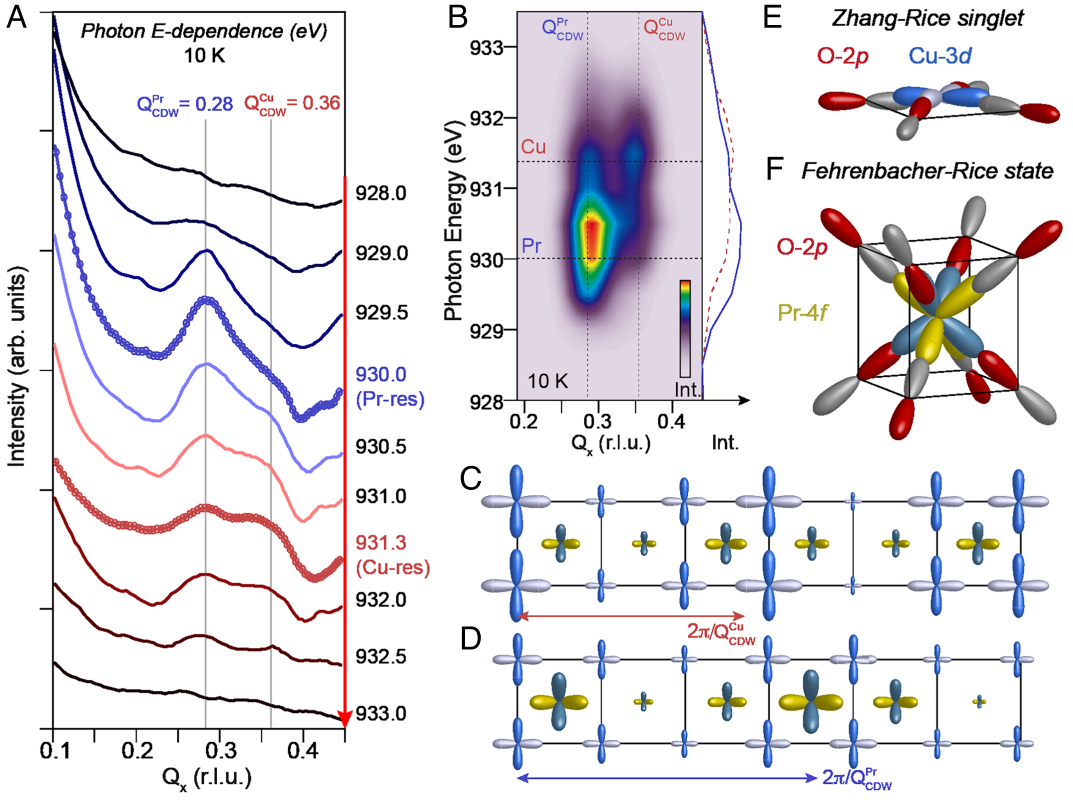

Fig. 2. Resonant profile of CDW and hybridization between Pr-4*f* and CuO_2 orbitals in PrBCO. (*A*) Photon energy-dependence of the X-ray scattering data (momentum scans) for positive Q_x. The curves are vertically shifted for clarity. Two curves with data points marked with open circles highlight the RXS scans at the peak of the Pr- and Cu-resonances. (*B*) Intensity map representing the resonant behavior of CDW after subtraction of the fluorescence background. The red-dashed and blue-solid curves on the right show the resonant profile at Q^{Cu}_{CDW} and Q^{Pr}_{CDW}, respectively. (*C* and *D*) Schematics of the two density-waves with different Cu-3*d* and Pr-4*f* orbital contents. The orbitals at the corner and center of the unit cell represent the Cu-3*d* and Pr-4*f* orbitals, respectively. (*E*) Schematic of the Zhang-Rice singlet state formed upon hybridization of planar Cu-$3d_{x2-y2}$ orbital and O-2*p* hole states. (*F*) Schematic of the Fehrenbacher–Rice state formed upon hybridization of Pr-$4f_{z(x2-y2)}$ orbital and surrounding O-2*p* hole states.

The correlation length, polarization dependence, and ordering axis of these diffraction signatures are all consistent with the characteristics of in-plane CDWs in other cuprates, while the presence of multiple ordering peaks requires further investigation.

To understand these initial observations, we turn to the photon energy dependence of the RXS spectra. As shown in Fig. 2*A*, the two main diffraction peaks display a surprising evolution with photon energy. When X-rays are tuned more than 2 eV away from the Pr and Cu resonances, the peaks vanish (see the profiles at 928.0 and 933.0 eV for examples), indicating that the diffraction signatures arise from valence band electronic modulations within the CuO_2-Pr-CuO_2 bilayer. A similar dual-resonance at both the Pr-M_5 and Cu-L_3 edges is also reported for a 3D CDW in $x = 0.3$ YPrBCO at $L = 1$ (47). Despite our scattering geometry probing different momentum-space (near $L = 1.5$, see *Material and Methods*), the dual-resonance in both cases confirms the active role of Pr-4*f* orbitals and validates our strategy of using Pr-doping to modify the electronic ground state of YBCO.

As can be seen in the intensity color map of Fig. 2*B*, the first diffraction peak, hereafter termed Q_{CDW}^{Pr}(≈0.28 r.l.u.), resonates at the Pr-edge, while the second peak Q_{CDW}^{Cu}(≈0.36 r.l.u. for $x = 0$) is most prominent at the Cu-edge (931.3 eV). The RXS data shown in Fig. 2 indicate the presence of two electronic modulations in PrBCO. First, the Q_{CDW}^{Pr} peak can be ascribed to a spatial modulation of the Pr-4*f* orbital occupation (see schematics in Fig. 2*D*). We interpret this signal as arising from Pr_{4f}-O_{2p_π} hybridized valence states (Fig. 2*F*) which have been proposed within the Fehrenbacher–Rice model (36). Second, the Q_{CDW}^{Cu} peak corresponds to a periodic modulation of the electronic density in the Cu-$3d_{x^2-y^2}$ orbitals (Fig. 2 *C* and *E*) and is thus closely related to the in-plane CDW observed in $YBCO_{7-y}$.

To validate this connection, we examine the evolution of our RXS profile for YPrBCO from the superconducting ($x = 0$, 0.275, and 0.5) to insulating ($x = 0.75$, 1) regimes, as shown in Fig. 3*A*. For superconducting YBCO ($x = 0$), the Cu-resonant CDW order appears at $Q_{CDW}^{Cu} \approx 0.3$ r.l.u., in agreement with previous studies of $YBCO_{7-y}$ (10). For intermediate Pr-doping levels $x = 0.275$ and $x = 0.5$, we still observe a single CDW peak resonating at the Cu-L_3 edge, with Q_{CDW}^{Cu} shifting to ≈ 0.32 and 0.33 r.l.u., respectively (*SI Appendix*, Figs. S5 and S6). For $x \geq 0.75$ in the insulating regime, the double-peak structure begins to appear, with $Q_{CDW}^{Cu} \approx 0.36$ r.l.u.. Compared to the continuous increase of Q_{CDW}^{Cu} with Pr-doping, the Q_{CDW}^{Pr} slightly decreases from 0.29 r.l.u. in $x = 0.75$ to 0.28 r.l.u. in $x = 1$ (Fig. 3 *A* and *B*). The observed doping dependence of Q_{CDW}^{Pr} may constrain the underlying mechanism of the charge modulation in the Pr-4*f* states (Fig. 2*D*), which requires future theoretical investigations.

In contrast to the complex evolution of CDW in YPrBCO, the RXS profiles for EuBCO and HoBCO films, which serve as control samples in this study, show only a single CDW peak at nearly the same position as Q_{CDW}^{Cu} for YBCO (*SI Appendix*, Fig. S4 for detailed characterization of charge order in EuBCO and HoBCO). This similarity indicates that rare-earth 4*f* orbitals generally play a passive role in the in-plane CDW of *R*BCO, with the clear exception of Pr-substitution.

The increase of Q_{CDW}^{Cu} with Pr-doping *x* observed in YPrBCO (Fig. 3*A*) corresponds to a linear evolution across the entire range of hole concentration *p*. To show this in Fig. 3*B*, we first plot our Q_{CDW}^{Cu} data for $x = 0$, 0.275 and 0.5 (red circles) as a function of *p*, which is determined from T_c and *x* using the formula: $1 - T_c/(T_{c,max} - 97x) = 82.6(p-0.16)^2$ (see details in *SI Appendix*). This formula is adapted for YPrBCO from the established T_c vs. *p* relation for $YBCO_{7-y}$ (32, 48), by adding a $-97x$ term to $T_{c,max}$ to account for its reduction due to Pr-doping, as deduced by Neumeier *et al.* via Ca-counterdoping (33, 40). Next, we plot the Q_{CDW}^{Cu} data (diamonds) taken on $YBCO_{7-y}$ from ref.

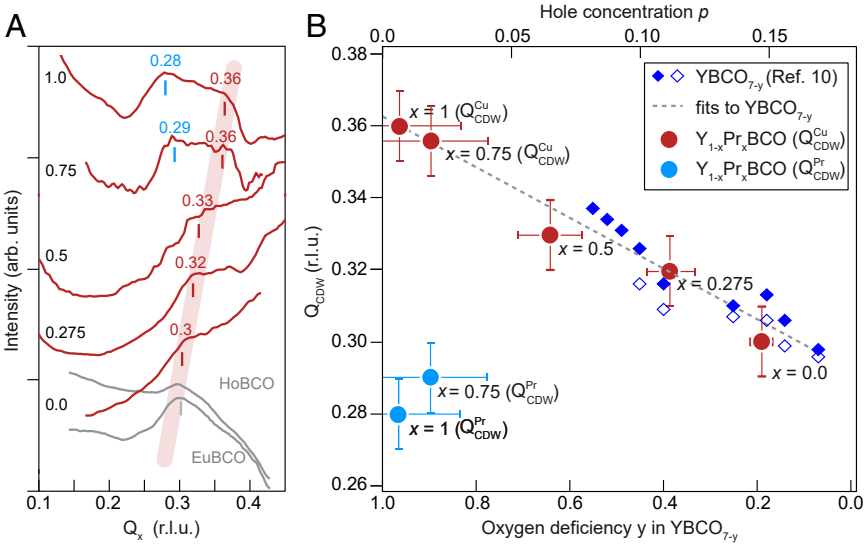

Fig. 3. Evolution of the in-plane CDW wave vector Q_{CDW} versus doping. (*A*) RXS profiles taken on YPrBCO films as a function of Pr-doping *x* (labeled on the *Left*). The position of Q_{CDW}^{Cu} is indicated by red bars. Data for the HoBCO and EuBCO control samples are shown as gray curves. A red shade highlights the evolution of Q_{CDW}^{Cu} as Pr-doping increases. The position of Q_{CDW}^{Pr} for the $x = 0.75$ and 1.0 films is indicated by cyan bars. (*B*) Q_{CDW} vs. hole concentration *p* for YPrBCO and $YBCO_{7-y}$. Blue diamonds represent data for $YBCO_{7-y}$ adapted from ref. 10, where open/filled symbols correspond to *a*/*b*-axis and the gray dashed line is a linear fit of Q_{CDW}^{Cu} vs. *p*. Red circles represent our data for YPrBCO. The *p* positions of the superconducting ($x = 0.0$, 0.275, 0.5) samples are determined using a modified T_c vs. *p* formula (see main text) and corroborate the linear relationship between Q_{CDW}^{Cu} and *p*. The *p* positions of the insulating ($x = 0.75$, 1.0) samples are determined by plotting their Q_{CDW}^{Cu} on a linear extension of the Q_{CDW}^{Cu} vs *p* relationship. Q_{CDW}^{Pr} data for the $x = 0.75$ and 1.0 films are plotted as blue circles.

10, along with a linear fit represented by a gray dotted line, to show that our YPrBCO data (red circles) follow the same linear evolution versus p in the metallic doping regime. Finally, we extrapolate this linear fit to the $p = 0$ limit, and plot our Q_{CDW}^{Cu} data for $x = 0.75$ and 1 along the fit line, to show that the linear evolution vs. p plausibly extends into the insulating regime. This extension indicates that, similar to oxygen-underdoping, Pr-doping monotonically reduces p toward zero to the Mott limit, consistent with the insulating and magnetic ground state of our PrBCO ($x = 1$) sample. The reduction also agrees with the published XAS data for YPrBCO (37), which showed essentially no holes in the Zhang-Rice band for $x > 0.8$.

To complete the characterization of charge order in our YPrBCO films, we also explored their temperature dependence. In PrBCO, the diffraction signatures from the Cu and Pr states display different dependences on temperature. As shown in *SI Appendix*, Fig. S5, the resonant scattering intensity I_{CDW}^{Pr} clearly decreases with increasing temperature, while I_{CDW}^{Cu} evolves more gradually all the way up to 300 K (*SI Appendix*, Fig. S5). This difference suggests that, while coexisting, these two modulated states are independent as can be expected from their association to different degrees of freedom (21–28). Similar to the temperature dependence of the 3D CDW reported in ref. 47, both I_{CDW}^{Pr} and I_{CDW}^{Cu} are still present up to at least 300 K. We also note that the very gradual evolution of I_{CDW}^{Cu} in PrBCO is reminiscent of the temperature dependence of charge density fluctuations seen in ref. 49 and therefore could suggest a partly fluctuating nature of the observed spatial modulations. At intermediate doping levels, the temperature evolution of I_{CDW}^{Cu} shows a very gradual onset of the CDW signal at around 200 to 250 K (*SI Appendix*, Fig. S5), higher than the onset temperatures observed in $YBCO_{7-y}$ (10).

Discussion

Fig. 4 summarizes our results in an updated phase diagram for YPrBCO, showing regions associated with several types of order: 1) antiferromagnetism of the Cu spins, as well as low-temperature ordering of the Pr spins (red dotted line), both evidenced by our μSR data (Fig. 1 *F* and *G*) in accordance with refs. 38, 50, and 51; 2) superconductivity, as confirmed by our transport measurements (Fig. 1*E*) and consistent with refs. 38 and 50; and 3) charge-ordered phases in both the metallic and insulating regimes as observed in our RXS data (Figs. 2 and 3). In addition, the gray squares denote T^*, which are determined from nonlinearity onsets in our resistivity vs. temperature data and associated with the pseudogap order (see *SI Appendix*, Fig. S7 and references therein).

This phase diagram reveals the persistence of charge modulations in both metallic ($x = 0$, 0.275, 0.5) and insulating ($x = 0.75$ and 1) regimes of YPrBCO. At the same time, we emphasize several phenomenological differences between the charge orders in these two regimes. First, the charge modulation emerges from the metallic background and coexists with superconductivity in the $x = 0$, 0.275, 0.5 films, while that in the $x = 0.75$ and 1 films emerges from the insulating background and coexists with the static spin orders. Second, the Cu-site modulation Q_{CDW}^{Cu} cohabits with the Pr-site modulation Q_{CDW}^{Pr} only in the latter films. Finally, the charge order onsets below $T_{CDW} = 100 \sim 250$ K in $x = 0$, 0.275, 0.5 films, while the charge order intensity is almost temperature-independent in $x = 0.75$, 1 films and persists above the room temperature. In sum, the charge modulation in the metallic regime broadly resembles the CDW seen in other underdoped cuprates, while that in the insulating

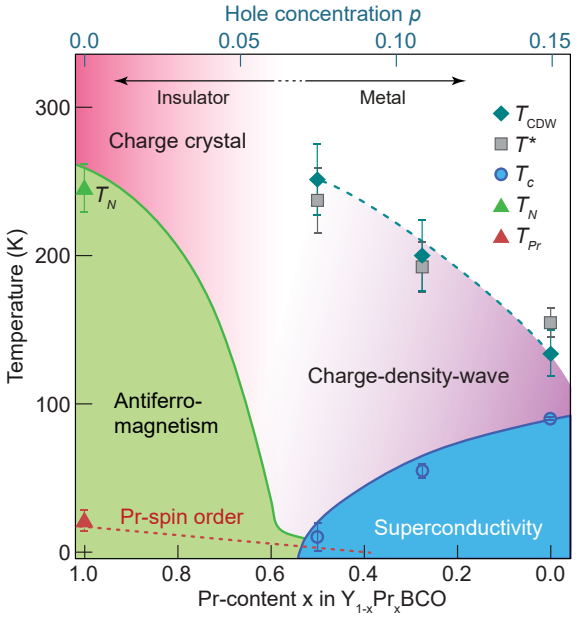

Fig. 4. Updated phase diagram of YPrBCO. The green region denotes antiferromagnetic order of the Cu spins, and the red dotted line marks the onset of low-temperature Pr spin order. Both are observed in our μSR measurements (Fig. 1 *F* and *G*) and in accordance with refs. 38, 50, and 51. The blue region denotes superconductivity, confirmed by our transport measurement (Fig. 1*E*) and consistent with refs. 38 and 50. The cyan region denotes the metallic CDW phase, and the magenta region denotes the insulating CDW phase (also termed "charge crystal"), both observed in our RXS data (Figs. 2–5). Gray squares mark the pseudogap onset temperature T^*, as determined from nonlinear deviations in our resistivity data (*SI Appendix*, Fig. S7).

films is reminiscent of the charge crystal phase recently observed in the insulating surface of Bi-based cuprates (31).

We discuss other noteworthy features in the YPrBCO phase diagram presented above. First, the CDW phase boundary rises monotonically with Pr-doping (Fig. 4), in contrast to the domed boundary of the in-plane CDW for oxygen-underdoped YBCO (Fig. 1*B*). Concomitantly, superconducting transition temperature is suppressed smoothly with Pr-doping without the 1/8 anomaly observed in the YBCO phase diagram. Also noteworthy is the apparent coevolution of T_{CDW} and T^* with decreasing p in Fig. 4, which is distinct from their diverging evolution in Fig. 1*B*. Further studies are needed to elucidate what these distinct features of the YPrBCO phase diagram imply about the fundamental relationships between the different types of order in high-T_c cuprates. Most importantly, our study reveals a charge order in the CuO_2 planes that pervades the entire doping range of the cuprate phase diagram, all the way to the Mott limit. Combined with the recent observation of charge modulations on an insulating surface of $Bi_2Sr_2CaCu_2O_{8+z}$ (31), our results support the existence of a common "charge crystal" phase emerging in the strongly correlated ground state of lightly doped CuO_2 planes.

Regarding the origin of CDWs in cuprates, two main viewpoints have been adopted over the years (21–28): the real space Coulomb-frustration scenario and the momentum-space instability scenario. These competing hypotheses have been invoked to successfully explain different aspects of the CDW phenomenology in cuprates. The present results offer important insights and constraints in this context: The observation of a spatially-modulated electronic phase in the insulating limit is fundamentally incompatible with the scenarios that rely on the presence of the low-energy itinerant states, which are broadly termed the momentum-space instability scenario (26–28). In-

stead, the prediction of the charge crystal phases assisted by the long-range Coulomb interactions in the very lightly doped antiferromagnetic insulators (i.e., real-space Coulomb-frustration scenario) is compatible with the magnetic insulating ground state of PrBCO (3, 21, 22).

Materials and Methods

Pulsed Laser-Ablated Deposition of YPrBCO Thin Films. YPrBCO thin films were epitaxially grown along the *c*-axis using pulsed laser-ablated deposition (PLD). To optimize in-plane lattice matching, films with $x \leq 0.5$ were grown on $(LaAlO_3)_{0.3}(Sr_2TaAlO_6)_{0.7}$ (LSAT) substrates and films with $x > 0.5$ on $SrTiO_3$ (STO) substrates. PLD growth was done using a 248 nm KrF excimer laser with a fluence of 2 J/cm^2. Films were grown using 200 mTorr O_2 chamber pressure and substrate temperatures of 750 °C to 800 °C. Further details of the PLD growth process are given in ref. 52. All the films grown had a nominal thickness of 40 nm, which was set using target-specific growth rates. The growth rates were determined using atomic force microscopy, by measuring the step heights of test films after they were chemically etched to create a step edge. The films are expected to be ≈50 % twinned, following the results of other similarly grown YBCO films (53).

Plasma-Assisted Reactive Sputter Deposition of HoBCO and EuBCO Films. HoBCO and EuBCO films were deposited on LSAT (100), polished single crystal substrates. The substrates were heated from 825 °C during deposition. A DC magnetron sputtering source was used with 50 mm HoBCO and EuBCO stoichiometric targets that had been verified by XRD. The chamber during growth was 330 mTorr with an argon to oxygen ratio of 1.5 sccm. Once the chamber settings were stable the DC magnetron sputter gun was ignited and ramped up to 55 watts over the course of 10 min. Typical growth rates were around 1 nm/min with a final film thickness of 55 nm. After deposition, the chamber was filled with 500 Torr of ultrahigh purity oxygen and allowed to stand at deposition temperatures for 10 min. After, power was cut from the heater and the samples were allowed to cool to room temperature in 500 Torr of oxygen. The critical temperatures were 92 to 94 K with a current density of 3 MA/cm^2 at 77 K. Electrical transport measurements for HoBaCuO Josephson devices are reported here (54).

XRD and Transport Characterization of YPrBCO Films. The as-grown films were characterized using XRD and resistance vs. temperature (R vs. T) measurements. XRD measurements were done using the θ–2θ method and show the expected substrates and films. The R vs. T measurements were done in a He-4 cryostat using an AC resistance bridge and silver contacts in the Kelvin configuration. Superconducting transitions were observed in the $x = 0.275$ and $x = 0.5$ films, and insulating behavior in the $x = 0.75$ and $x = 1.0$ films. The critical temperatures (T_c) and R vs. T behaviors are similar to other YPrBCO films of comparable Pr and oxygen doping (38, 55–57). Similarly grown YBCO films were shown to be epitaxially bonded to the substrate using transmission electron microscopy (TEM) in a previous study (58).

Resonant X-ray Scattering Experiments. RXS experiments were performed in two different beamlines, the UE46-PGM1 beamline of BESSY II at Helmholtz Zentrum Berlin ($x = 0$, 0.275, and 1) and the REIXS (10ID-2) beamline of Canadian Light Source ($x = 0.5$, 0.75). All RXS measurements were conducted in ultrahigh vacuum diffractometers with the pressure better than 10^{-9} torr. Samples were aligned in situ using (0 0 2) and (1 0 2) Bragg diffractions. Momentum-space scans were obtained by rocking the sample angle θ around 110° or 50° at a fixed detector position $2\theta = 160°$. This scattering geometry measures the RXS spectra around the transferred in-plane momentum 0.3 r.l.u. or −0.3 r.l.u. and out-of-plane momentum 1.5 r.l.u. X-ray absorption spectra (XAS) were measured by monitoring total electron yields. We used out-of-scattering-plane (σ) polarizations for both RXS and XAS measurements unless specified.

Muon Spin Spectroscopy Experiments. The low-energy μSR experiments were performed at the μE4 beamline (59) which is part of the Swiss Muon Source, Paul Scherrer Institut, Villigen, Switzerland. The μSR data have been analyzed with the help of MUSRFIT (60). Details about the μSR technique can be found in ref. 61. All the measurements were conducted in ultrahigh vacuum at a pressure smaller than 10^{-8} mbar and zero magnetic field conditions. The decay positron asymmetry spectra were analyzed with the function $A(t) = A_{osc}\cos(\gamma_\mu B_{int} t + \phi)\cdot e^{-\lambda_T t} + A_1\, e^{-(\lambda_L t)^\beta}$, where A_{osc} is the coherent zero field oscillation amplitude, γ_μ is the muon gyromagnetic ratio, B_{int} the internal magnetic field at the muon site, and ϕ is the phase between the initial muon spin direction and the decay positron detector. $\lambda_{T,L}$ are the transverse and longitudinal depolarization rates. $\beta \simeq 1$ except close to the phase transition where it is close to 2.

Data, Materials, and Software Availability. All study data are included in the article and/or supporting information.

ACKNOWLEDGMENTS. This work was supported by the Air Force Office of Scientific Research Young Investigator Program under grant FA9550-19-1-0063 and National Research Foundation of Korea, Ministry of Science, Grant No. 2022M3H4A1A04074153. Work at the University of Toronto was supported by the Natural Sciences and Engineering Research Council (NSERC) through the Discovery Grant and the Alliance International Catalyst Quantum Grant, and by the Canada Foundation for Innovation (CFI). Part of the research described in this paper was performed at the Canadian Light Source, a national research facility of the University of Saskatchewan, which is supported by CFI, NSERC, the National Research Council, the Canadian Institutes of Health Research, the Government of Saskatchewan, and the University of Saskatchewan. M.K. acknowledges a Samsung Scholarship from the Samsung Foundation of Culture.

Author affiliations: [a]Department of Physics, Massachusetts Institute of Technology, Cambridge, MA 02139; [b]Center for Complex Phase of Materials, Max Planck POSTECH/Korea Research Initiative, Pohang 790-884, Republic of Korea; [c]Department of Physics, University of Toronto, Toronto, ON M5S1A7, Canada; [d]Helmholtz-Zentrum Berlin für Materialien und Energie, Berlin D-12489, Germany; [e]Department of Materials Science and Engineering, University of California, Riverside, CA 92521; [f]Department of Electrical Engineering, University of California, Riverside, CA 92521; [g]Canadian Light Source, Saskatoon, SK S7N 2V3, Canada; and [h]Laboratory for Muon-Spin Spectroscopy, Paul Scherrer Institut, Villigen CH-5232, Switzerland

Author contributions: J.Y.T.W. and R.C. designed research; M.K., C.C.Z., E.S., S.M., J.L., R.S., A.S., T.P., Z.S., E.W., S.C., J.Y.T.W., and R.C. performed research; M.K., C.C.Z., E.S., J.L., R.S., J.Y.T.W., and R.C. analyzed data; E.S., R.S., and E.W. maintained the beamlines and RXS endstations; J.Y.T.W. and R.C. codirected the project; and M.K., C.C.Z., J.Y.T.W., and R.C. wrote the paper.

1. J. G. Bednorz, K. A. Müller, Possible highT superconductivity in the Ba-La-Cu-O system. *Z. Phys. B Condens. Matter* **64**, 189 (1986).
2. M. K. Wu *et al*., Superconductivity at 93 K in a new mixed-phase Y-Ba-Cu-O compound system at ambient pressure. *Phys. Rev. Lett.* **58**, 908 (1987).
3. J. Zaanen, O. Gunnarsson, Charged magnetic domain lines and the magnetism of high-Tc oxides. *Phys. Rev. B* **40**, 7391 (1989).
4. K. Machida, Magnetism in La2CuO4 based compounds. *Physica C* **158**, 192 (1989).
5. D. Poilblanc, T. M. Rice, Charged solitons in the Hartree–Fock approximation to the large-/U Hubbard model. *Phys. Rev. B* **39**, 9749 (1989).
6. V. J. Emery, S. A. Kivelson, H. Q. Lin, Phase separation in the t-J model. *Phys. Rev. Lett.* **64**, 475 (1990).
7. J. M. Tranquada, B. J. Sternlieb, J. D. Axe, Y. Nakamura, S. Uchida, Evidence for stripe correlations of spins and holes in copper oxide superconductors. *Nature* **375**, 561 (1995).
8. G. Ghiringhelli *et al*., Long-range incommensurate charge fluctuations in (Y, Nd)Ba2Cu3O6+x. *Science* **337**, 821 (2012).
9. J. Chang *et al*., Direct observation of competition between superconductivity and charge density wave order in YBa2Cu3O6.67. *Nat. Phys.* **8**, 871 (2012).
10. S. Blanco-Canosa *et al*., Resonant X-ray scattering study of charge density wave correlations in YBa2Cu3O6+x. *Phys. Rev. B* **90**, 054513 (2014).
11. R. Comin *et al*., Charge order driven by Fermi-arc instability in Bi2Sr2-xLaxCuO6+d. *Science* **343**, 390 (2014).
12. E. H. da Silva Neto *et al*., Ubiquitous interplay between charge ordering and high temperature superconductivity in cuprates. *Science (New York, N.Y.)* **343**, 393 (2014).
13. W. Tabis *et al*., Charge order and its connection with Fermi-liquid charge transport in a pristine high-Tc cuprate. *Nat. Commun.* **5**, 5875 (2014).
14. E. H. da Silva Neto *et al*., Charge ordering in electron doped superconductor Nd2-xCexCuO4. *Science* **347**, 282 (2015).

15. E. H. da Silva Neto *et al*., Doping dependent charge order correlations in electron-doped cuprates. *Sci. Adv.* **2**, e1600782 (2016).
16. M. Kang *et al*., Evolution of charge order topology across a magnetic phase transition in cuprate superconductors. *Nat. Phys.* **15**, 335 (2019).
17. R. Comin, Resonant X-ray scattering studies of charge order in cuprates. *Annu. Rev. Condens. Matter Phys.* **7**, 369 (2016).
18. S. A. Kivelson *et al*., How to detect fluctuating stripes in the high-temperature superconductors Rev. *Mod. Phys.* **75**, 1201 (2003).
19. J. M. Tranquada, Exploring intertwined orders in cuprate superconductors. *Physica B* **460**, 136 (2015).
20. E. Fradkin, S. A. Kivelson, J. M. Tranquada, Colloquium: Theory of intertwined orders in high temperature superconductors. *Rev. Mod. Phys.* **87**, 457 (2015).
21. S. Kivelson, E. Fradkin, V. Emery, Electronic liquid-crystal phases of a doped Mott insulator. *Nature* **393**, 550 (1998).
22. M. Vojta, S. Sachdev, Charge order, superconductivity, and a global phase diagram of doped antiferromagnets. *Phys. Rev. Lett.* **83**, 3916 (1999).
23. S. Sachdev, R. La Placa, Bond order in two-dimensional metals with antiferromagnetic exchange interactions. *Phys. Rev. Lett.* **111**, 027202 (2013).
24. J. C. S. Davis, D.-H. Lee, Concepts relating magnetic interactions, intertwined electronic orders and strongly correlated superconductivity. *Proc. Natl. Acad. Sci. U.S.A.* **110** (2013).
25. P. A. Lee, Amperean pairing and the pseudogap phase of cuprate superconductors. *Phys. Rev. X* **4**, 031017 (2014).
26. Y. Wang, A. Chubukov, Charge density wave order with momentum (2Q,0) and (0,2Q) within the spin-fermion model: Continuous and discrete symmetry breaking, preemptive composite order, and relation to pseudogap in hole-doped cuprates. *Phys. Rev. B* **90**, 35149 (2014).
27. E. G. Dalla Torre, Y. He, D. Benjamin, E. Demler, Exploring quasiparticles in high-Tc cuprates through photoemission, tunneling, and X-ray scattering experiments. *New J. Phys.* **17**, 22001 (2015).
28. L. Q. Duong, T. Das, Correlation between Fermi arc and charge order resulting from the momentum-dependent self-energy correction in cuprates. *Phys. Rev. B* **96**, 125154 (2017).
29. B. Keimer, S. A. Kivelson, M. R. Norman, S. Uchida, J. Zaanen, From quantum matter to high-temperature superconductivity in copper oxides. *Nature* **518**, 179 (2015).
30. S. A. Kivelson, E. Fradkin, V. J. Emery, Electronic liquid-crystal phases of a doped Mott insulator. *Nature* **393**, 550 (1998).
31. H. Zhao *et al*., Charge-stripe crystal phase in an insulating cuprate. *Nat. Mater.* **18**, 103 (2019).
32. R. Liang, D. A. Bonn, W. N. Hardy, Evaluation of CuO2 plane hole doping in YBa2Cu3O6+x single crystals *Phys. Rev. B* **73**, 180505(r) (2006).
33. J. J. Neumeier, T. Bjornholm, M. B. Maple, I. K. Schuller, Hole filling and pair breaking by Pr ions in $Y_{1-x}Pr_xBa_2Cu_3O_{6.95\pm0.02}$. *Phys. Rev. Lett.* **63**, 2516 (1989).
34. A. G. Sun, L. M. Paulius, D. A. Gajewski, M. B. Maple, R. C. Dynes, Electron tunneling and transport in the high-t_c superconductor $Y_{1-x}Pr_xBa_2Cu_3O_{7-\delta}$. *Phys. Rev. B* **50**, 3266 (1994).
35. W. Y. Guan, Y. C. Chen, J. Y. T. Wei, Y. H. Xu, M. K. Wu, Ion-size effect on T_m and T_c in $(R_{1-x}Pr_x)Ba_2Cu_3O_7$ systems (R = Yb, Tm, Er, Ho, Dy, Gd, Eu, Sm, Nd and Y). *Physica C* **209**, 19 (1993).
36. R. Fehrenbacher, T. M. Rice, Unusual electronic structure of PrBa2Cu3O7. *Phys. Rev. Lett.* **70**, 3471 (1993).
37. M. Merz *et al*., X-ray absorption spectroscopy of detwinned $(Pr_x)Y_{1-x}Ba_2Cu_3O_{7-y}$ single crystals: Electronic structure and hole distribution. *Phys. Rev. B* **55**, 9160 (1997).
38. H. B. Radousky, A review of the superconducting and normal state properties of Y1-xPrxBa2Cu3O7. *J. Mater. Res.* **7**, 1917 (1992).
39. D. P. Norton *et al*., Transport and structural properties of $Pr_{1-x}Ca_xBa_2Cu_3O_{7-\delta}$ thin films grown by pulsed-laser deposition. *Phys. Rev. B* **49**, 4182 (1994).
40. J. J. Neumeier, M. B. Maple, Superconducting critical temperature and electrical resistivity of the system $Y_{1-x}Pr_xBa_2Cu_3O_{6.95}$ ($0 \leq x \leq 1$). *Physica C* **191**, 158 (1992).
41. A. Frano *et al*., Long-range charge density wave proximity effect at cuprate/manganate interfaces. *Nat. Mater.* **15**, 831 (2016).
42. R. S. Liu *et al*., Induced superconductivity in tetragonal $YBa_2Cu_3O_6$ by incorporation of Ca. *Solid State Commun.* **76**, 679 (1990).
43. S. K. Tolpygo, J.-Y. Lin, M. Gurvitch, S. Y. Hou, J. M. Phillips, Effect of oxygen defects on transport properties and T_c of $YBa_2Cu_3O_{\delta+x}$: Displacement energy for plane and chain oxygen and implications for irradiation-induced resistivity and T_c suppression. *Phys. Rev. B* **53**, 12462 (1996).
44. D. W. Cooke *et al*., Magnetic ordering in $(Y_{1-x}Pr_x)Ba_2Cu_3O_7$ as observed by muon-spin relaxations. *Phys. Rev. B* **41**, 4801(R) (1990).
45. L. Soderholm *et al*., Incorporation of Pr in YBa2Cu3O7-d: Electronic effects on superconductivity. *Nature* **328**, 604 (1987).
46. B. M. Wojek *et al*., Magnetism, superconductivity, and coupling in cuprate heterostructures probed by low-energy muon-spin rotation. *Phys. Rev. B* **85**, 024505 (2012).
47. A. Ruiz *et al*., Stabilization of three-dimensional charge order through interplanar orbital hybridization in $Pr_xY_{1-x}Ba_2Cu_3O_{6+\delta}$. *Nat. Commun.* **13**, 1–7 (2022).
48. J. L. Tallon, C. Bernhard, H. Shaked, R. L. Hitterman, J. D. Jorgensen, Generic superconducting phase behavior in high-T_c cuprates: T_c variation with hole concentration in $YBa_2Cu_3O_{7-\delta}$. *Phys. Rev. B* **51**, 12911(R) (1995).
49. R. Arpaia *et al*., Dynamical charge density fluctuations pervading the phase diagram of a Cu-based high-Tc superconductor. *Science* **365**, 906 (2019).
50. M. Akhavan, The question of Pr in HTSC. *Physica B* **321**, 265 (2002).
51. J. P. Hill, X-ray-scattering study of copper magnetism in nonsuperconducting PrBa2Cu3O6.92. *Phys. Rev. B* **61**, 1251 (2000).
52. H. Zhang *et al*., Synthesis of high-oxidation Y-Ba-Cu-O phases in superoxygenated thin films. *Phys. Rev. Mater.* **2**, 33803 (2018).
53. P. Paturi, M. Peurla, K. Nilsson, J. Raittila, Crystalline orientation and twin formation in YBCO thin films laser ablated from a nanocrystalline target. *Supercond. Sci. Technol.* **17**, 564 (2004).
54. S. J. McCoy, E. Y. Cho, H. Li, S. A. Cybart, "Ho-Ba-Cu-O thin films for superconductive electronics" in *IEEE International Superconductive Electronics Conference* (2019), p. 1.
55. R. V. Vovk, Z. F. Nazyrov, I. L. Goulatis, A. Chroneos, Metal-to-insulator transition in Y1-xPrxBa 2Cu3O7-δ single crystals with various praseodymium contents. *Physica C* **485**, 89 (2013).
56. L. Antognazza *et al*., Layer by layer preparation of YPBCO alloy thin films. *J. Less Common Metals* **165**, 344 (1990).
57. J. L. Peng *et al*., Upper critical field and normal-state properties of single-phase YPBCO compounds. *Phys. Rev. B* **40**, 4517 (1989).
58. H. Zhang, N. Gauquelin, G. A. Botton, J. Y. Wei, Attenuation of superconductivity in manganite/cuprate heterostructures by epitaxially-induced CuO intergrowths. *Appl. Phys. Lett.* **103**, 052606 (2013).
59. T. Prokscha *et al*., The new μe4 beam at psi: A hybrid-type large acceptance channel for the generation of a high intensity surface-muon beam. *Nuclear Inst. Methods Phys. Res. Sec. A: Acceler. Spect. Detect. Assoc. Equip.* **595**, 317 (2008).
60. A. Suter, B. Wojek, Musrfit: A free platform-independent framework for μSR data analysis. *Phys. Procedia* **30**, 69 (2012).
61. A. Yaouanc, P. Dalmas de Réotier, *Muon Spin Rotation, Relaxation, and Resonance* (Oxford University Press, 2011).